Applied Catalysis B: Environmental 174–175 (2015) 157–166

Contents lists available at ScienceDirect

Applied Catalysis B: Environmental

journal homepage: www.elsevier.com/locate/apcatb

# Design of a neutral photo-electro-Fenton system with 3D-ordered macroporous $Fe_2O_3$/carbon aerogel cathode: High activity and low energy consumption

Qiusheng Peng, Hongying Zhao*, Lin Qian, Yanbin Wang, Guohua Zhao*

*Department of Chemistry, and Shanghai Key Lab of Chemical Assessment and Substainability, Tongji University, 1239 Siping Road, Shanghai 200092, China*

ARTICLE INFO

*Article history:*
Received 6 January 2015
Received in revised form 12 February 2015
Accepted 21 February 2015
Available online 24 February 2015

*Keywords:*
3D ordered marcoporous
$Fe_2O_3$
Photo-E-Fenton
Carbon aerogen electrode
Imidacloprid

ABSTRACT

A novel three-dimensional ordered macroporous $Fe_2O_3$/CA cathode (3DOM–$Fe_2O_3$/CA) was fabricated by using self-assembled colloidal crystal template and proposed in solar photo-electro-Fenton (SPEF) process at neutral pH. 3DOM–$Fe_2O_3$/CA possessed 3D-ordered interconnecting marcopores (390–425 nm) with a hollow "cylindrical tube" in the vertical direction. Compared to the traditional $Fe_2O_3$/CA electrode, the 3DOM–$Fe_2O_3$/CA presented higher photocatalytic and Fenton oxidation ability. The interconnecting macropores generated multiple scattering and slow-photon effect for increasing light harvesting efficiency, while the nice channels minimized tortuosity and provided much more efficient mass transport. Almost complete removal of 200 mg $L^{-1}$ imidacloprid was achieved in 2.5 h with 3DOM–$Fe_2O_3$/CA. The dynamic analysis showed that the degradation of imidacloprid follows the pseudo-first order reaction. The apparent rate constant for 3DOM–$Fe_2O_3$/CA electrode is 0.326 $h^{-1}$, which 2 times higher than that of reference $Fe_2O_3$/CA electrode. The energy consumption was used more effectively in SPEF with 3DOM–$Fe_2O_3$/CA. EPR and radical trapping experiments revealed that the •OH radicals were main oxidants in SPEF system and 3D-ordered macroporous favored the formation of •OH. Besides, 3DOM–$Fe_2O_3$/CA electrode presented very low iron leaching (<1 ppm) and retained high catalytic activity after consecutive runs.



## 1. Introduction

In recent years, the focus on waste minimization and water conservation leads to the discovery of kinds of treatment processes, one of them being electro-Fenton (EF) oxidation technology [1–3]. This process is of interest since it opens up a green approach to electrochemical utilization of air as a sustainable source for oxygen supply [4]. It is based on the continuous electrogeneration of $H_2O_2$ via a two-electron reduction of $O_2$ at the cathode. Then the $H_2O_2$ is decomposed with Fenton catalysts to generate hydroxyl radicals (•OH), which has very high standard reduction potential ($E^{\theta}$(•OH/$H_2O$) = 2.80 V) versus SHE) that non-selectively and efficiently decomposes most organics [5–9]. Therefore the efficiency of electro-Fenton (EF) for removing pollutants mainly depends on the generation ability of $H_2O_2$ with cathode materials [10] and the decomposition ability of $H_2O_2$ with Fenton catalysts [5]. In addition, many EF requires an optimum pH of ≤3 especially for homogeneous system, and a certain amount of $Fe^{2+}$ and the effluent must be neutralized after such treatment process. That is to say, the acidic condition and iron sludge disposal would greatly limit the application of electro-Fenton treatment [11,12]. Accordingly, developing novel heterogeneous electro-Fenton catalysts with high catalytic efficiency at neutral pH would be very important.

The principal factor determining catalytic efficiency in heterogeneous catalysis are the exposed active site and the sufficiently large surface area, which can be achieved by the use of either nanoparticles or granular particles with porous character [13]. That is to say, the catalytic efficiency of EF can be improved through modifying the structure of heterogeneous catalysts. Moreover, the oxidation ability of EF can be significantly enhanced by illuminating the treated effluent with UV light or sunlight [2,14]. The coupling of Fenton method with photocatalysis system is another way to enhance its decontamination efficiency [2,15]. Iron (III) oxide, inexpensive, environmentally and sufficient utilize ~40% of the incident sunlight, has been extensively studied due to its potential applications in the field of photo-electro-Fenton (PEF) process [16]. However, the catalytic ability of traditional $Fe_2O_3$ in PEF is quite limited

* Corresponding authors. Tel.: +86 21 65981180; fax: +86 21 65982287.
*E-mail addresses:* hyzhao@tongji.edu.cn (H. Zhao), g.zhao@tongji.edu.cn (G. Zhao).

http://dx.doi.org/10.1016/j.apcatb.2015.02.031
0926-3373/

especially at neutral pH. Three-dimensionally (3D) ordered materials have been attracted considerable interests as heterogeneous catalysts [17–20]. Their well-defined and ordered marcropores can provide nice channels to minimize toruosity and enhance mass transport. Besides, the 3D marcropores can also improve the light harvesting efficiency through multiple scattering and slow photons effect [17]. The improved photocatalytic ability can further improve the Fenton activity of $Fe_2O_3$ by accelerating the circulation of $Fe^{II}/Fe^{III}$ during EF reaction.

So, the degradation efficiency of SPEF system would be greatly enhanced if 3DOM–$Fe_2O_3$ catalysts can be introduced on a proper cathode substrate. The ideal cathode material in EF should meet the following characteristics: (i) high surface area with good adsorption ability, (ii) high electrical conductivity and electrochemical active reaction area (iii) high-efficiency for producing $H_2O_2$. The bulk carbon aerogel (CA), representative of novel porous electrode materials, presents three-dimensional (3D) network structure, high specific surface area and good electrical conductivity [21,22], which would be a promising cathode substrate for EF process.

On the other hand, how to make the electro-Fenton process energy more effective is highly desirable especially in actual treatment [23]. The energy supply should be minimized while the reaction rate of EF reaction for pollutant degradation should be increased [24]. A process using sunlight ($\lambda > 300$ nm) as a renewable and inexpensive energy source, the called solar PEF(SPEF), is a much more appealing alternative [23]. Thus, in this work, we proposed to introduce novel $Fe_2O_3$ with highly ordered three-dimensional macroporous to aerogel carbon substrate (3DOM–$Fe_2O_3$/CA electrode). So far, the fabrication and applicaton of 3DOM–$Fe_2O_3$/CA cathode in heterogeneous solar photo-electro-Fenton (SPEF) for wastewater treatment at neutral pH is rarely reported. Imidacloprid (IMI), [1-(6-chloronicotinyl)-2-nitroimino-imidazolidine], is the archtypal member of representative chemical of the neonicotinoid insecticide family, and one of the insecticides most used in agricultural areas [25], was selected as a model pollutant for evaluating the catalytic activity of this novel cathode. The main purpose of this work is to elucidate the effect of 3D-ordered macroporous on the heterogeneous electro-Fenton and photocatalytic activity at neutral pH. In addition, a plausible enhanced reaction mechanism with novel 3DOM–$Fe_2O_3$/CA electrode in SPEF oxidation of IMI was also proposed.

## 2. Experimental

### 2.1. Reagents and materials

Monodisperse polystyrenelatex spheres (ac. 502 nm, 2.5 wt% in water) were purchased as a suspension from Shenzhen Nanomicro Tech. China. 5,5-Dimethylpyrroline-1-oxide (DMPO) was obtained from Aladdin Industrial Corporation. Resorcinol, formaldehyde, sodium carbonate, acetone, iron nitrate ($Fe(NO_3)_3{\cdot}9H_2O$), polyvinylpyrrolidone(PVP), sodium hydroxide, imidacloprid were obtained from Aladdin Co., China. Ethylalcohol, methanol, isopropanol, hydrochloric acid, sodium sulfate were purchased from Sinopharm (Shanghai, China). All of the chemicals were analytical grade and used without further purification except that methanol is chromatographic grade. All solutions were prepared with deionized water.

### 2.2. Preparation of 3DOM–$Fe_2O_3$/CA cathode

Synthesis of CA. The preparation method of carbon aerogels electrode was based on our previously reported literatures [26,27]. Resorcinol, formaldehyde, deionized water were mixed with a molar ratio of 1:2:14.3. After forming a homogeneous solution, the mixture was transfer into a cuboid glass case (4cm × 3cm × 1 cm) with the interlayer distance of 5 mm, and then sealed and cured at 30 °C for one day, 50 °C for one day, and 90 °C to polymerize and age, resulting in metallic-organic wet gel and CA former body, respectively. The as-prepared gel was immersed in acetone for 3 days to exchange the water in the former body and then dried under ambient conditions to obtain a massive dry gel with integrated structure. Finally, it was carbonized in a tubular oven at 950 °C for 4 h in argon atmosphere with the flow rate of 100 mL $min^{-1}$.

Synthesis of 3DOM–$Fe_2O_3$/CA. The polystyrene sphere colloidal crystal film was self-assembled on CA by in situ solvent evaporation method [28]. Firstly, in a 10 mL weighing bottle, the CA was vertically immersed in the polystyrene spheres (PS, average diameter about 502 nm) suspension with a concentration of 2.5 wt% (sonicated for 30 min to disperse before using). The weighing bottle was kept in an oven at 45 °C until the water in the suspension was completely evaporated, and a colorized polystyrene opals film was assembled to the carbon aerogel substrate (PS/CA). Secondly, theoretical amount of $Fe(NO_3)_3{\cdot}9H_2O$ was dissolved in absolute ethanol to form a homogeneous solution (1 M), and then the PS/CA electrode was vertically immersed in the above-mentioned precursor solution until ethanol was fully volatilized at room temperatures. Finally, the PS template was removed in quartz tube furnace in argon atmosphere at 500 °C for 2 h, obtaining the 3DOM–$Fe_2O_3$/CA electrode. The traditional reference $Fe_2O_3$/CA electrode was prepared refer to the same procedure without PS photonic crystal as template.

### 2.3. Characterization methods

The macroporous structure and morphologies of the electrode were investigated by scanning electron microscope (EFEG-SEM, Model Quanta 200 FEG, FEI) with an accelerating voltage of 3 kV. The X-ray diffraction (XRD, D/max2550VB3 + /PC, Rigaku) measurements were performed making use of adiffractometer with Cu Kα radiation. Raman spectra were obtained on a Raman spectrometer (Renishaw Crop., UK) using a He/Ne laser with the wavelength of 515 nm. The surface area and pore size of the samples were tested after heat treatment under vacuum at 573 K for 3 h by the BET adsorption–desorption isotherms at 77 K using a Micromeritics 3000 apparatus. The amount (wt%) of $Fe_2O_3$ loaded on 3DOM–$Fe_2O_3$/CA and $Fe_2O_3$/CA surface was determined from ignition loss in air at 1000 °C by using comprehensive thermal analysis apparatus [29]. UV–vis diffuse reflection spectroscopy (UV–vis DRS, JASCO V-550) was applied to determination of light absorption properties of the electrode.

### 2.4. Electrochemical property test

All of the electrochemical properties were conducted in electrochemical workstation with three electrode system (CHI 660D Shanghai Chenhua Instrument Co., Ltd., China). The Pt foil acted as the reference electrode and a saturated calomel electrode (SCE) as the counter electrode, while the 3DOM–$Fe_2O_3$/CA and traditional $Fe_2O_3$/CA served as the work electrode, respectively. The electrochemical impedance spectroscopy (EIS) was used to determine the conductivity of catalysts at the open circuit potential, with the frequency range from $1 \times 10^5$ to $1 \times 10^{-3}$ Hz and amplitude 5 mV, and the electrolyte was 0.1 M $Na_2SO_4$ solution.

### 2.5. Degradation experiment and analysis

The solar photo-electro-Fenton oxidation of imidacloprid (IMI) was carried out in a cylindri-cal single compartment cell equipped with air-blowing device and a jacketed cooler to retain a constant temperature. The light source was a 500 W Xe lamp. A 100 mL

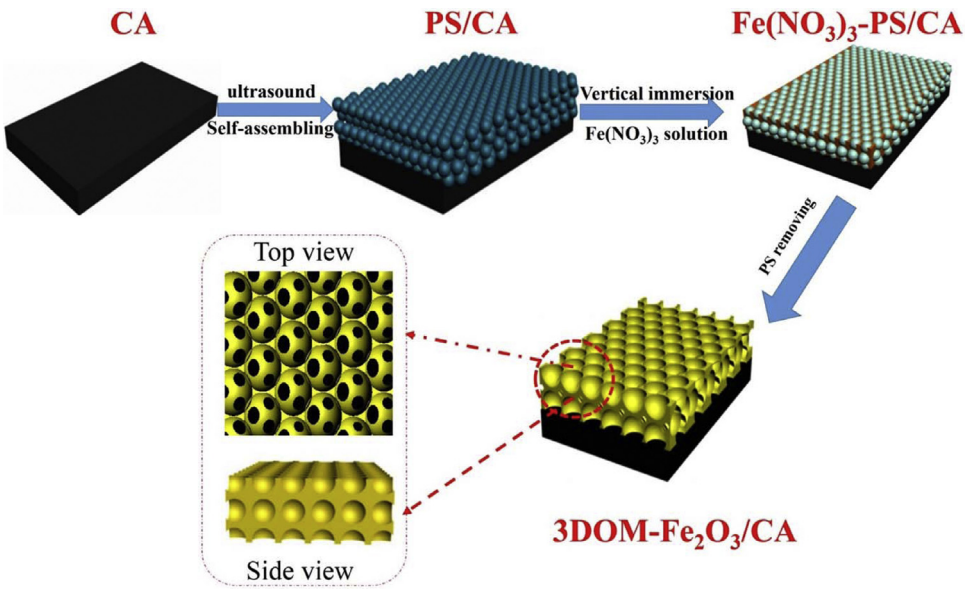


**Fig. 1.** Schematic illustration of the fabrication of 3DOM–$Fe_2O_3$/CA electrode.

200 ppm imidacloprid in $Na_2SO_4$ (0.1 M) solution served as the simulated wastewater. The 3DOM–$Fe_2O_3$/CA and reference $Fe_2O_3$/CA electrodes (working area of 3 $cm^2$) worked as the cathode, respectively, and a BDD acted as the anode with the same area, while the distance between the two electrodes is 2 cm. Air was fed onto the cathode surface at a flow rate of 300 mL $min^{-1}$. The optimal operative current density was maintained to be constant at 10 mA $cm^{-2}$, and the relevant potential was with 2.85 V [30].

The IMI concentration during the degradation was measured by high-performance liquid chromatography (HPLC, Agilent HP1100) equipped with a reverse phase AQ-C18 column (4.6 mm × 250 mm, particles size 5 μm) and a UV detector. The detection wavelength was set at 270 nm, and the mobile phase was a mixed solution of 30% methanol and 70% water (V/V).

ESR spectra were obtained on a Bruker EMX Xplus-10/12 with Microwave Bridge (microwave frequency, 9.853 GHz; microwave power, 20 mW; modulation amplitude, 1 G; modulation frequency, 100 kHz). For ESR measurement, 50 μL of the sample was collected form the suspension system which was mixed with theoretical DMPO to form DMPO-•OH adduct [31]. The determination of $H_2O_2$ was performed by using titanium oxysulfate as indicator and UV–vis spectrophotometer (Agilent 8453, Agilent Corporation, U.S.) was used to measure the absorbance of the complex compound solution at the maximum absorption wavelength λ = 409 nm [26]. The concentration of leached iron was measured with 1,10-phenantrolinemethod by recording the absorbance at 510 nm [32]. The samples were measured using an Agilent 8453 UV–vis spectrophotometer with a 1 cm path length spectrometric quartz cell. The total organic carbon (TOC) concentration was determined using a TOC analyzer (TOC-Vcpn, Shimadzu, Japan). TOC values were determined by a Multi 3100 TOC/TN analyzer.

## 3. Results and discussion

### 3.1. The fabrication, structural and photoelectrochemical properties of novel 3DOM–$Fe_2O_3$/CA electrode

The 3DOM–$Fe_2O_3$/CA electrode was fabricated by the combination with sol–gel method and hard template (PS spheres) method based on self-assembled photonic crystal [33]. The construction process is schematically illustrated in Fig. 1. The preparation process includes the following steps: firstly, CA substrate was synthesized according to a modified ambient drying technique described in our previous work [27,34], including sol–gel formation, solvent exchange, ambient pressure drying and pyrolysis [35]. Secondly, the CA was vertically immersed in 500 nm PS suspension at 45 °C until the water was completely evaporated for obtaining PS-coated CA electrode (PS/CA). Since the roughness of CA surface, it is difficult to fabricate PS colloidal crystal with a well-ordered, periodic and crack-free macroporous structure. To solve the problem, ultrasonic treatment was introduced and multilayer deposition of PS was constructed to achieve smooth surface. In this case, the PS was organized into a close-packed arrangement with long-range order both parallel and perpendicular to substrate. Thirdly, the obtained PS/CA electrode was again vertically immersed into $Fe(NO_3)_3$ ethanol solution until ethanol was completely volatilized at room temperatures. Iron-based ions continuously and homogeneously permeated into the voids between the spheres and can be further decomposed in situ. Finally, highly ordered inverse opal structured $Fe_2O_3$ outer was obtained after calcination at 500 °C for 2 h in argon atmosphere. During this process, PS template was removed and $Fe(NO_3)_3$ was simultaneously hydrolyzed into $Fe_2O_3{\cdot}xH_2O$. After all the above mentioned procedures, three dimensional (3D) ordered macroporous electrode 3DOM–$Fe_2O_3$/CA was obtained.

Fig. 2 shows SEM images of the substrate CA, 3DOM–$Fe_2O_3$/CA and traditional $Fe_2O_3$/CA electrodes. As exhibited in Fig. 2A, the CA has a three-dimensional network of interconnected carbon particles with the diameter of 20–50 nm and a large percentage of pores. In another word, the surface of CA was extremely coarse and uneven. After immersing CA into PS suspension, uniform PS spheres with diameter of 500 nm can be self-assembled in hexagonally close-packed crystals on CA surface (PS/CA) (see Fig. 2B). The top view of the SEM image for 3DOM–$Fe_2O_3$/CA electrode is presented in Fig. 2C and D. The top surface was composed of a three dimensionally ordered, closely packed, hexagonal $Fe_2O_3$ array. The average macropore size of 3D-ordered $Fe_2O_3$ was reduced to 390–425 nm, which show 15–22% shrinkage in comparison with the primary PS spheres. A cross-section SEM image as shown in Fig. 2E and F presented well-defined vertically ordering (~10 layers). Interesting, the holes with the diameter of ~120 nm in each layer formed a hollow "cylindrical tube" in the vertical direction (Fig. 2F), which would be favorable for

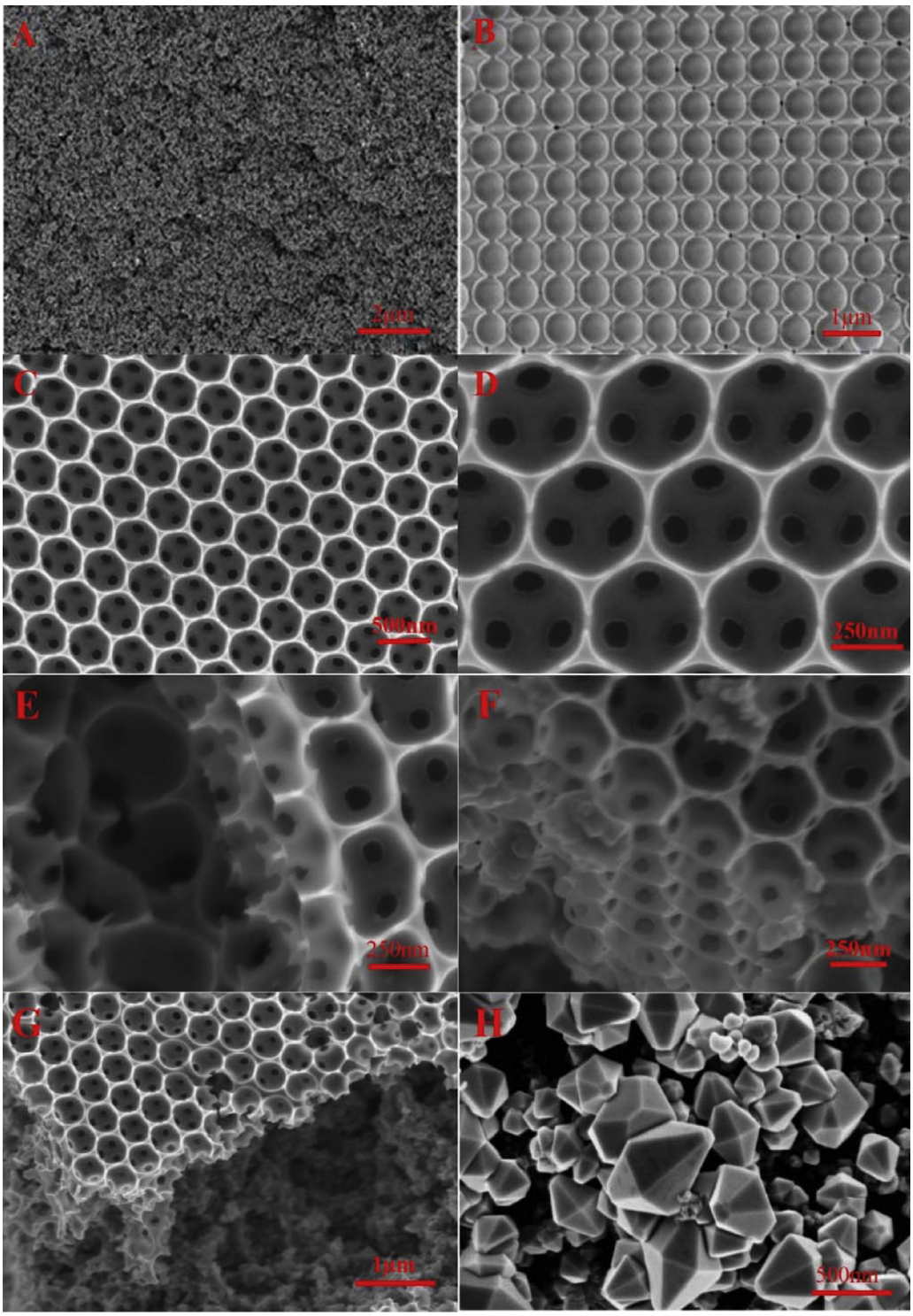


**Fig. 2.** SEM images of (A) CA substrate; (B) self-assembled PS photonic crystal on the CA substrate; (C)–(G) as-prepared 3DOM–$Fe_2O_3$ on the CA substrate, (H) traditional $Fe_2O_3$ on the CA substrate.

enhancing the diffusion and mass transport of pollutants. As shown in Fig. 2G, CA substrate was clearly presented on the bottom of 3DOM $Fe_2O_3$ arrays. In addition, as one of the reference sample, traditional $Fe_2O_3$ with large crystal size was also prepared (Fig. 2H). Comparing to reference $Fe_2O_3$, the 3D-ordered interconnecting marcopores in 3DOM $Fe_2O_3$/CA provided very nice channels that can minimize tortuosity and allowed much more efficient mass transport for reactants to reach on $Fe_2O_3$ framework wall and for products to leave from the active sites to solution [36].

XRD patterns of the as-prepared 3DOM–$Fe_2O_3$/CA and traditional $Fe_2O_3$/CA electrodes are presented in Fig. 3. Typical diffraction peaks characteristic of α-$Fe_2O_3$ at 24.1°, 33.1°, 35.7°, 40.9°, 49.5°, 54.0°, 62.4° and 64.0° were obtained. Additionally, these peaks were consistent with the diffraction of the (0 1 2), (1 0 4), (1 1 0), (1 1 3), (0 2 4), (1 1 6), (2 1 4) and (3 0 0) planes of

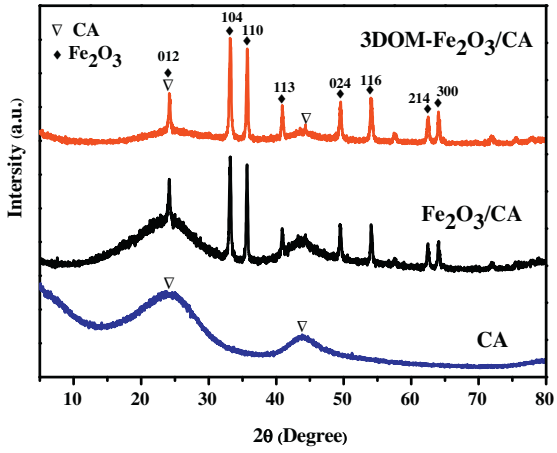


**Fig. 3.** XRD patterns of as-prepared 3DOM–$Fe_2O_3$/CA and $Fe_2O_3$/CA electrodes.

hematite $Fe_2O_3$ (JCPDS89-8103). The reflection peaks at 24.1° and 44.1° were indexed to CA substrate. To get further insight on the structure of 3DOM–$Fe_2O_3$/CA electrode, a Raman study was also carried out, as shown in Fig. 4. Both 3DOM–$Fe_2O_3$/CA and common $Fe_2O_3$/CA has five intense vibrating peaks at 217 $cm^{-1}$, 281 $cm^{-1}$, 394 $cm^{-1}$, 489 $cm^{-1}$ and 585 $cm^{-1}$ corresponding to the α-$Fe_2O_3$. Simultaneously, it appears one vibrating peak at 1340 $cm^{-1}$ amount to graphite crystallite D of CA.

The amount of $Fe_2O_3$ in the 3DOM–$Fe_2O_3$/CA and $Fe_2O_3$/CA cathodes was evaluated by TG analysis. As shown in Fig. 5, for 3DOM–$Fe_2O_3$/CA, a significant weight loss beginning at 500 °C due to the oxidation of CA substrate to $CO_2$. In addition, substrate CA was completely converted to $CO_2$ at 800 °C. While for traditional $Fe_2O_3$/CA cathode prepared by hydrothermal method, a similar weight loss between 500 and 800 °C was also observed. Besides, another slight weight loss appeared before 500 °C, which is mostly due to the decomposition of water existing in the pore of CA. By calculating the mass loss, the loading amount of the 3DOM–$Fe_2O_3$ and $Fe_2O_3$ can be determined as about 15 wt% and 16 wt%, respectively.

The physic-chemical properties of obtained electrodes were also characterized in detail, and the corresponding parameters are listed in Table 1. The BET surface area and pore volume of pure CA was 744 $m^2\ g^{-1}$ and 0.277 $m^3\ g^{-1}$, respectively. After incorporating $Fe_2O_3$, the $S_{BET}$ of common $Fe_2O_3$/CA and 3DOM–$Fe_2O_3$/CA was declined to 512 and 540 $m^2\ g^{-1}$, while the pore volume of the two electrode was, respectively, decreased to 0.200 and 0.203 $m^3\ g^{-1}$. 3DOM–$Fe_2O_3$/CA possessed relatively higher BET surface area than

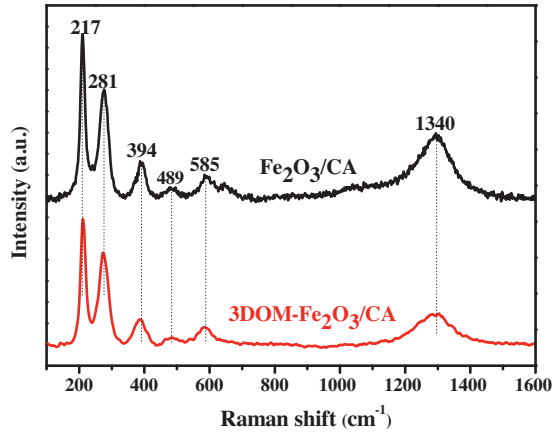


**Fig. 4.** Raman spectra of 3DOM–$Fe_2O_3$/CA and $Fe_2O_3$/CA elecrodes.

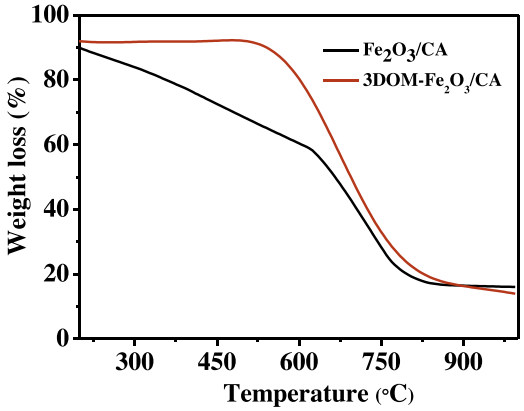


**Fig. 5.** TG/DTA analysis of 3DOM–$Fe_2O_3$/CA and $Fe_2O_3$/CA electrodes in air atmosphere.

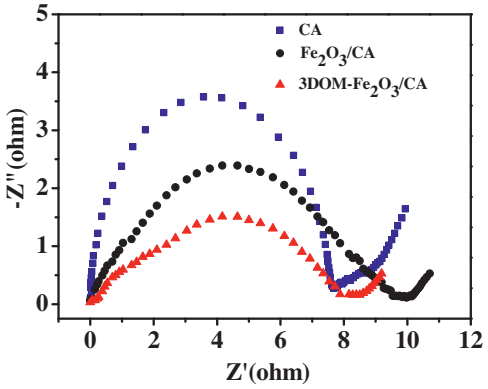


**Fig. 6.** Electrochemical impedance spectroscopy of CA, $Fe_2O_3$/CA and 3DOM–$Fe_2O_3$/CA electrodes.

common $Fe_2O_3$/CA electrode, which is mostly due to the high quality 3D-ordered marcopores structured $Fe_2O_3$.

Moreover, an ideal E-Fenton electrode should not only have Fenton catalytic activity but also needs excellent electrochemical properties. Fig. 6 presents the electrochemical impedance spectroscopy of used electrodes. The physical resistance of CA is 2.5 Ω $cm^{-1}$ (see Fig. 6) and the electrochemical impedance of CA is 7.8 Ω (see Table 1), indicating that substrate CA has excellent conductivity. After loading $Fe_2O_3$, the physical resistance of 3DOM–$Fe_2O_3$/CA and $Fe_2O_3$/CA electrodes was, respectively, increased to 8.6 and 9.0 Ω $cm^{-1}$. And the electron transfer resistance for 3DOM–$Fe_2O_3$/CA and $Fe_2O_3$/CA was respectively increased to 9.0 and 9.7 Ω, anyhow, still presenting good conductivity. In addition, 3DOM–$Fe_2O_3$/CA electrode presented low resistivity than $Fe_2O_3$/CA, suggesting that the three-ordered macroporous structure decreased the resistance of electrochemical action, promoted electron transport and would reduce the corresponding energy consumption.

The diffuse reflectance UV–vis spectroscopy of 3DOM–$Fe_2O_3$/CA and $Fe_2O_3$/CA sample were tested, as shown in Fig. 7. Both electrodes exhibited strong absorption bands in visible region. The

**Table 1**
Comparison of physico-chemical parameters for different electrodes.

| Sample | CA | 3DOM–$Fe_2O_3$/CA | $Fe_2O_3$/CA |
|---|---|---|---|
| Specific surface area ($m^2\ g^{-1}$) | 744 | 540 | 512 |
| Pore volume ($m^3\ g^{-1}$) | 0.277 | 0.203 | 0.200 |
| Resistance (Ω $cm^{-1}$) | 2.5 | 8.6 | 9.0 |
| Electrochemical impedance (Ω) | 7.8 | 9.0 | 9.7 |

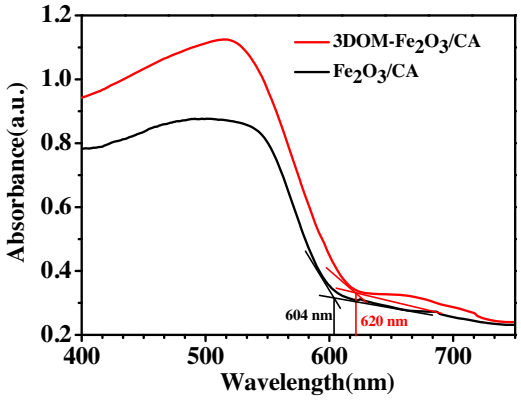


**Fig. 7.** UV–vis diffuse reflectance spectra of 3DOM–$Fe_2O_3$/CA and $Fe_2O_3$/CA electrodes.

absorption oneset of the spectrum for $Fe_2O_3$/CA is 604 nm, and the band gap is about 2.05 eV, in agreement with previous reported values [17]. As for novel 3DOM–$Fe_2O_3$/CA, an obvious red-shift of the band gap adsorption edge was observed from 604 to 620 nm. Additionally, 3DOM–$Fe_2O_3$/CA exhibited stronger absorption intensity than reference $Fe_2O_3$/CA. These observations can be explained by two facts that (i) 3D-ordered macroprous structure increased the optical path with multiple scattering effect [37], and then enhanced light harvesting efficiency and (ii) small size $Fe_2O_3$ in 3DOM–$Fe_2O_3$/CA avoided the short diffusion length of photogenerated valence holes in reference $Fe_2O_3$ with large crystalline size [17,38].

### 3.2. Efficient degradation of imidacloprid with novel 3DOM–$Fe_2O_3$/CA electrode in SPEF oxidation process

The catalytic activity and removal efficiency on 3DOM–$Fe_2O_3$/CA cathode were evaluated by IMI degradation at neutral pH with initial concentration of 200 mg $L^{-1}$. The IMI removal is displayed in Fig. 8A, where different processes, electrosorption (ES), electro-Fenton (EF) and solar-photoelectro-Fenton (SPEF), were occurred on compared cathodes. In solo ES process a small potential is applied and the anode oxidation reaction scarcely happen. An approximately steady IMI removal, about 14%, is obtained with two cathodes at ES process due to the strong electrosorption capability of CA electrode. In EF process, the degradation efficiency of IMI with 3DOM–$Fe_2O_3$/CA was slightly higher than $Fe_2O_3$/CA cathode. For example, at 150 min, IMI removal was 69% and 63%, respectively, with the former and latter cathode. With the introducing of solar light irradiation, IMI degradation efficiency was greatly improved especially for novel 3DOM–$Fe_2O_3$/CA cathode. In SPEF process, at 150 min, IMI removal efficiency with 3DOM–$Fe_2O_3$/CA was increased to 95%, while for reference $Fe_2O_3$/CA, the degradation efficiency was increased to 74%.

In order to in-depth understand the photocatalytic ability of $Fe_2O_3$ and 3DOM–$Fe_2O_3$, a control experiment of solar light induced photocatalytic degradation of IMI was performed, as shown in Fig. 8B. Prior to the each experiment, nitrogen was filled into the system for 0.5 h to remove oxygen. The IMI oxidized efficiency, mostly induced by generated holes, with 3DOM–$Fe_2O_3$/CA was higher than $Fe_2O_3$/CA cathode. For instance, IMI removal was 24% and 19%, respectively, with the former and latter cathode at 150 min. Note that, the increase of photocatalytic ability in SPEF process with 3DOM–$Fe_2O_3$ was a litter higher than in pure PC process. This is due to that the formed $H_2O_2$ can be worked as electron acceptors and then promoted separation efficiency of generated $h^+$ and $e^-$, which would be deeply discussed in the mechanism section. Whatever, these observation indicated that the highly ordered 3D marcoprous structure of $Fe_2O_3$ possess higher photocatalytic activity than traditional $Fe_2O_3$ especially in SPEF process.

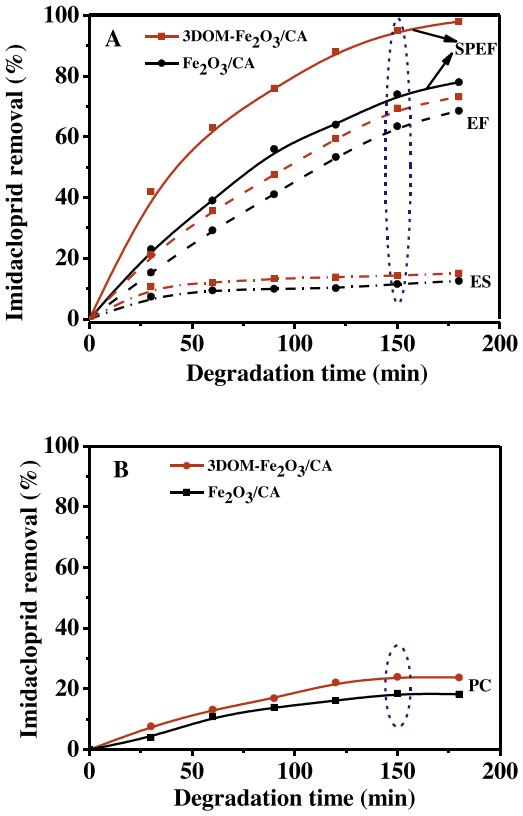


**Fig. 8.** The removal efficiency of imidacloprid with different electrodes in (A) ES, EF and SPEF processes, and (B) pure photocatlaytic (PC) process.

Moreover, the data for imidacloprid concentration decay in SPEF process with different cathodes were further analyzed by kinetic equation. The kinetics equation may be expressed as:

$$\ln\left(\frac{C_0}{C}\right) = kt$$

where $k$ is the apparent reaction constant and $C_0$ and $C$ are the initial concentration and the concentration at time $t$, of imidacloprid, respectively. The kinetic analysis shows that the degradation of IMI follows the pseudo-first order (see Fig. 9). The apparent rate constant ($k$) for 3DOM–$Fe_2O_3$/CA electrode is 0.326 $h^{-1}$, increased 97% by comparing to common $Fe_2O_3$/CA electrode (0.165 $h^{-1}$).

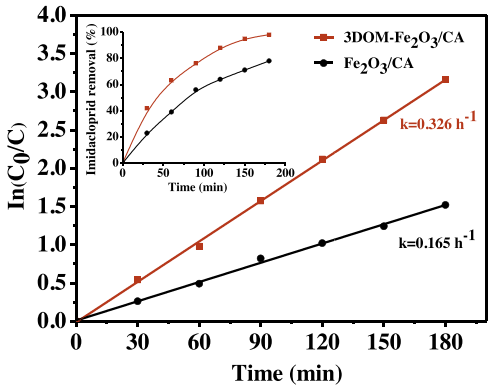


**Fig. 9.** The kinetic analysis of imidacloprid degradation in SPEF process with 3DOM–$Fe_2O_3$/CA and $Fe_2O_3$/CA eletrodes, that is dependence of $\ln(C_0/C)$ versus time.

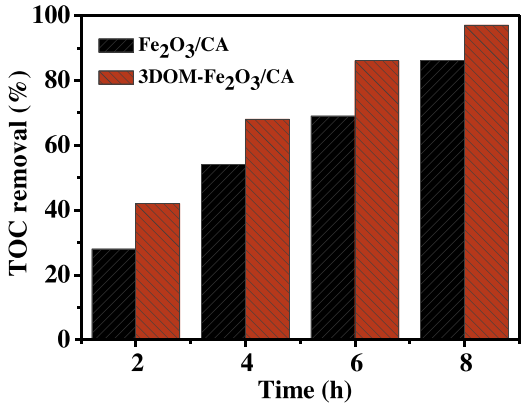


**Fig. 10.** TOC removal of imidacloprid with different electrodes at neutral pH and 200 mg $L^{-1}$ imidacloprid.

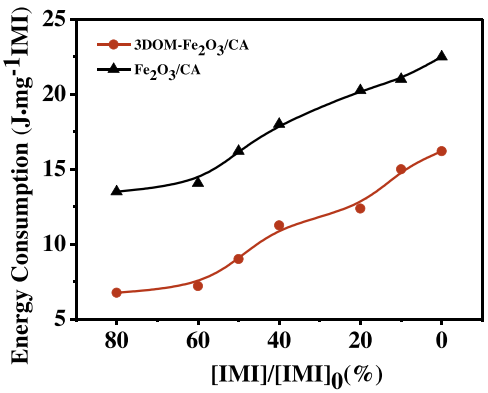


**Fig. 11.** The energy consumption in the process of IMI degradation with 3DOM–$Fe_2O_3$/CA and common $Fe_2O_3$/CA electrodes, $[IMI]_0$ = 200 mg $L^{-1}$, initial pH 7.

It is not enough to demonstrate the decontamination ability of catalysts only monitoring the primary pollutant removal efficiency, the determinations of TOC removal related to mineralization extent is also needed. As for example, the TOC removal in SPEF process at neutral pH with 3DOM–$Fe_2O_3$/CA and reference $Fe_2O_3$/CA electrode is shown in Fig. 10. The TOC removal was increased with increasing the degradation time, since the further decomposition of related intermediates with the proceeding of reaction. Obviously, novel 3DOM–$Fe_2O_3$/CA exhibited higher mineralization ability than reference electrode in this work. Its TOC removal was up to 98% at 8 h, which is 1.2 times higher than that of 80% for $Fe_2O_3$/CA electrode. Although TOC removal results again confirmed that the 3D-ordered macroporous structure with crystal defect sites and hollow "cylindrical tube" are favorable for improving photoelectric catalytic activity, it would be more meaningful if we can indicate the plausible enhanced catalytic mechanism and determine the key role improving the removal efficiency with novel 3DOM–$Fe_2O_3$/CA electrode.

The energy consumption (EC) is one of crucial parameters for evaluating the practicability of SPEF system from economic view. Thus, the EC for IMI degradation in SPEF process with different electrodes were calculated according to the following equation [4]:

$$\mathrm{EC}\left(\mathrm{kJ}\cdot\mathrm{mg}^{-1}\right) = \frac{U \times I \times t}{m_{\mathrm{IMI}}} \times 3600$$

where $U$ and $I$ are the cell voltage in voltage and the current in Ampere, respectively. $m_{IMI}$ is the amount of the degraded IMI in mg during the reaction time of $t$ in hour.

Fig. 11 shows the corresponding EC versus the IMI degradation percentage with 3DOM–$Fe_2O_3$/CA and $Fe_2O_3$/CA cathode in SPEF process. Obviously, the EC values gradually increased with the proceeding of IMI degradation reaction in all cases. Whereas, the EC values with 3DOM–$Fe_2O_3$/CA always lower than common $Fe_2O_3$/CA electrode through the whole reaction. For example, the EC values at 80% of $[IMI]/[IMI]_0$ for 3DOM–$Fe_2O_3$/CA is 12.3 kJ $mg^{-1}$, with respect to 20.3 kJ $mg^{-1}$ on common $Fe_2O_3$/CA electrode. This means the energy consumed in SPEF system with novel 3DOM–$Fe_2O_3$/CA could be used more effectively for IMI degradation.

### 3.3. Plausible enhanced reaction mechanism with novel 3DOM–$Fe_2O_3$/CA electrode in SPEF oxidation process

Based on the above observation, it is reasonable to say that the enhanced IMI removal and TOC removal in SPEF process with novel 3DOM–$Fe_2O_3$/CA electrode was mostly due to the improved Fenton catalytic and photocatalytic oxidation ability.

As shown in Fig. 12, the amount of $H_2O_2$ for both 3DOM–$Fe_2O_3$/CA and $Fe_2O_3$/CA increased with electrolysis time and then became almost constant after 120 min. The relatively low concentration of $H_2O_2$ in the first 90 min is due to that most of $H_2O_2$ were consumed by $Fe_2O_3$ via Fenton reaction. Besides, part of excess $H_2O_2$ would be anodically oxidized to $O_2$ ($H_2O_2 \rightarrow O_2 + 2H^+ + 2e^-$) or reacted with •OH that produced by BDD anode (BDD(•OH) + $H_2O_2 \rightarrow HO_2^{\bullet} + H_2O$) and Fenton reaction [39]. With the proceeding of SPEF reaction, most of IMI pollutant was removed and/or decomposed into intermediates, reducing the conversion rate of $H_2O_2$ to •OH through Fenton oxidation reaction. Moreover, the productivity of $H_2O_2$ with 3DOM–$Fe_2O_3$/CA electrode is higher than common $Fe_2O_3$/CA electrode. As we all know, substrate CA is an ideal electro-Fenton cathode material for in-situ generation of $H_2O_2$ since its porous structure. Comparing to reference $Fe_2O_3$/CA, the 3D-ordered interconnecting marcopores in 3DOM $Fe_2O_3$/CA provided very nice channels that can minimize tortuosity and allowed much more oxygen molecules transport to the CA surface to produce more $H_2O_2$.

The amount of •OH, formed by the catalytic decomposition of $H_2O_2$ with active sites on cathode, is strongly depending on the nature of Fenton catalysts, to some extent, can reflect the Fenton catalytic activity. Thus, the generation of •OH was monitored by EPR using 5,5-dimethypylpyrroline-1-oxide (DMPO) after reaction 20 min, as depicted in Fig. 13. The EPR spectrum with 3DOM–$Fe_2O_3$/CA and $Fe_2O_3$/CA both exhibited a 4-fold characteristic peak of the typical •OH/DMPO complex adduct with an intensity ratio of 1:2:2:1 [40]. With the identical lineshape of DMPO-adduct among used cathodes, the intensity can be directly related to the amount of generated •OH [41]. Obviously, the productivity of •OH with 3DOM–$Fe_2O_3$/CA electrode is around two times higher than

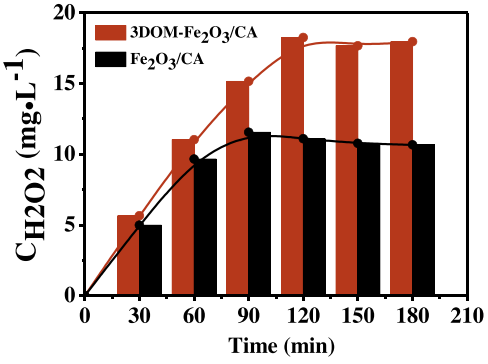


**Fig. 12.** $H_2O_2$ concentration evolution over 3DOM–$Fe_2O_3$/CA and $Fe_2O_3$/CA electrodes in SPEF system.

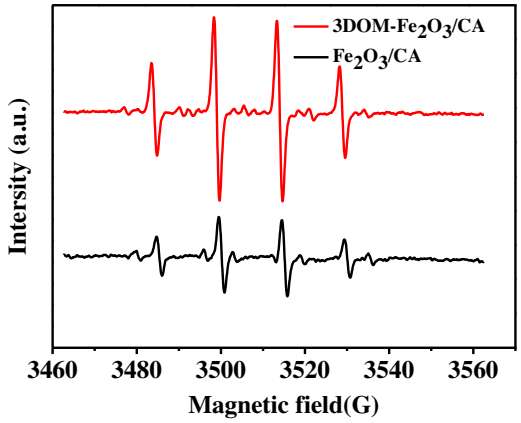


**Fig. 13.** DMPO spin trapping EPR Spectra over 3DOM–$Fe_2O_3$/CA and $Fe_2O_3$/CA electrodes in SPEF system.

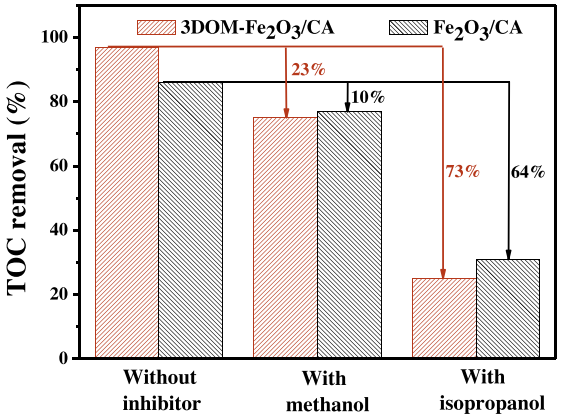


**Fig. 15.** Efffect of •OH radical and hole scavengers on TOC removal after reaction 8 h at neutral.

common $Fe_2O_3$/CA electrode, clearly indicating that the generation of •OH was greatly enhanced with 3D-ordered interconnecting marcopores in SPEF process.

To investigate the characteristics of 3DOM–$Fe_2O_3$/CA inverse opals as photocathode, photoelectrochemical analysis was carried out respectively with continuous feeding $N_2$ and $O_2$. As shown in Fig. 14, the photocurrent intensity of two electrodes was increased once turning on the visible light. Nevertheless, 3DOM–$Fe_2O_3$/CA electrode exhibited higher photocurrent intensity than common $Fe_2O_3$/CA electrode regardless of feeding gas, indicating higher light harvesting efficiency in the former than the latter. The interconnecting macropores in 3DOM–$Fe_2O_3$/CA generated multiple scattering and slow-photon effect for increasing the optical path in catalyst [17]. Besides to the light harvesting efficiency, the separation efficiency of electrons and holes is also very important for the whole the photocatalytic ability. Note that the photocurrent intensity of 3DOM–$Fe_2O_3$/CA electrode was decreased by 0.062 mA when feeding with $O_2$, which is two times larger than that of reference $Fe_2O_3$/CA (0.038 mA). This observation revealed that there are more generated electrons in 3DOM–$Fe_2O_3$/CA can be reacted with $O_2$, again suggesting that the 3D-ordered macroprous structure would accelerate the separation of generated electrons and holes under visible irradiation.

It is very important to determine the main oxidant in the photo E-Fenton process for investigating the reaction mechanism. Investigation the role of main oxidant could be carried out through radical and hole trapping experiments by using methanol (hole scavenger) [42] and isopropanol (radical scavenger) [43,44]. During the reaction, the amount of added scavenger was 1015 times

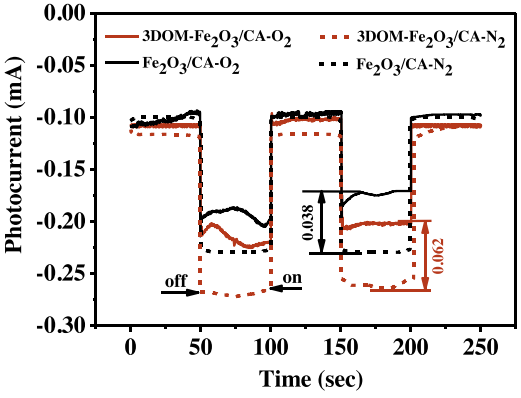


**Fig. 14.** Transient photocurrent responses of 3DOM–$Fe_2O_3$/CA and $Fe_2O_3$/CA with feeding $O_2$ and $N_2$ in 0.5 M $Na_2SO_4$ aqueous solutions under visible light irradiation.

greater than organic pollutant imidacloprid. As shown in Fig. 15, after adding hole scavenger methanol, around 23% and 10% inhibition on TOC removal were observed for 3DOM–$Fe_2O_3$/CA and reference $Fe_2O_3$/CA electrode, respectively. This observation confirmed that photogenerated holes were one kind of oxidants in SPEF process, which can play an important role on the oxidation of organic pollutants. Moreover, this observation also indicated that 3D-ordered macroprous structure in 3DOM–$Fe_2O_3$/CA would increase the concentration of generated holes and then enhance the photocatalytic ability. After adding isopropanol into reaction system, an obviously inhibitory effect was obtained on the TOC removal both for 3DOM–$Fe_2O_3$/CA (73%) and reference $Fe_2O_3$/CA (64%) electrodes. This not only suggested that the •OH radical presented as main participation in SPEF process but also revealed that the 3D-ordered macroprous structure favoring the formation of •OH, which is consisted with EPR results.

On the basis of the above experiments, a reasonable schematic mechanism for efficiently removing imidacloprid using 3DOM–$Fe_2O_3$/CA electrode in SPEF process was illustrated in Fig. 16. Firstly, active oxygen molecules were adsorbed on the surface of 3DOM–$Fe_2O_3$/CA cathode and then transformed to hydrogen peroxide through in situ reduction with two electrons captured in the circuit (Eq. (1)).

$$O_2 + 2H^+ + e^- \rightarrow H_2O_2 \quad (1)$$

Meanwhile, the surface iron species (Fe(II)–OH and Fe(III)–OH) would be interacted with formed $H_2O_2$ according with heterogeneous E-Fenton reaction mechanism (Eqs. (2)–(6)) [45–47]. For Fe(III)–OH, it was interacted with $H_2O_2$ to form a precursor surface complex of $H_2O_2$ as shown in Eq. (2). The surface $H_2O_2$ complex may further undergo a reversible ground-state electron transfer from ligand to metal (Eq. (3)), and then the successor complex would be decomposed through Eq. (4) to generate $HO_2^•$ oxidants. Note that in E-Fenton process, a potential in-situ recycling of iron species (Fe(III)–OH → Fe(II)–OH) would be easily happened through Eq. (5). For the converted Fe(II)–OH, it can directly reacted by $H_2O_2$ to generate •OH radicals and simultaneously be oxidized to Fe(III)–OH (Eq. (6)). That is why the main oxidant was still •OH radicals at neutral for $Fe_2O_3$ Fenton catalyst especially in E-Fenton process.

$$\equiv Fe^{III} - OH + H_2O_2 \rightarrow \equiv Fe^{III} - OH(HO_2^•)_{(s)} + H^+ \quad (2)$$

$$\equiv Fe^{III} - OH(H_2O_2)_{(s)} \rightarrow \equiv Fe^{II} - OH(HO_2^•)_{(s)} + H^+ \quad (3)$$

$$\equiv Fe^{II} - OH(HO_2^•)_{(s)} \rightarrow \equiv Fe^{II} - OH + HO_2^• + H^+ \quad (4)$$

$$\equiv Fe^{III} - OH + e^- \rightarrow \equiv Fe^{II} - OH \quad (5)$$

$$\equiv Fe^{II} - OH + H_2O_2 \rightarrow \equiv Fe^{III} - OH + {}^•OH + OH^- \quad (6)$$

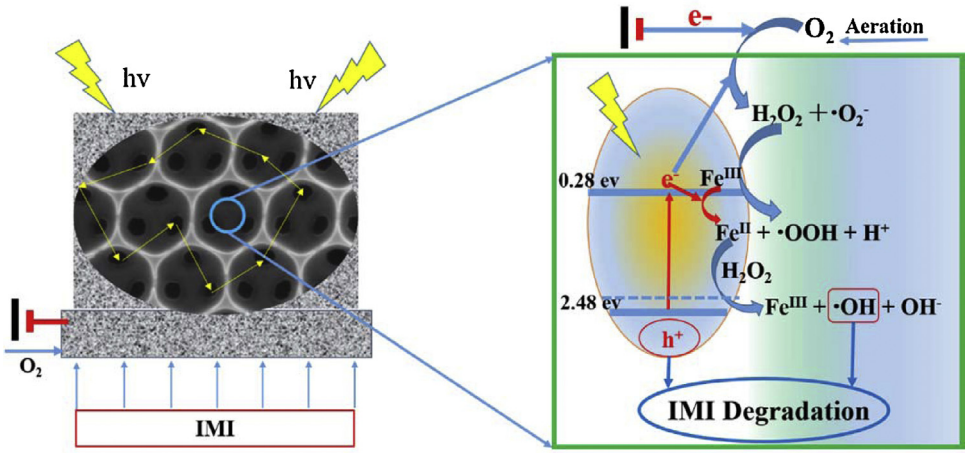


**Fig. 16.** Schematic illustration of efficiently degrading IMI with 3DOM–$Fe_2O_3$/CA electrode in SPEF process.

$$\cdot OH + IMI \rightarrow CO_2 + H_2O + \cdots \quad (7)$$

Moreover, since the 3D-ordered interconnecting marcopores structure, the separation efficiency of generated electrons and holes would be greatly enhanced, which indicating more electrons would be participated in Reactions (1) and (5) to generate more •OH radicals. 3DOM–$Fe_2O_3$/CA cathode also provided very nice channels that can minimize tortuosity and allow much more efficient mass transport for IMI reaching on electrode surface to be attacked with •OH (Eq. (7)).

On the other hand, as we known, the initial process of photocatalysis was the generation of electron–hole pairs in 3DOM–$Fe_2O_3$. Under visible light irradiation, the electrons ($e^-$) were excited from the valence band (VB) and entered into the conduction band (CB), leaving the holes ($h^+$) in the VB (Eq. (8)) [48]. As we mentioned above, 3D-ordered macroprous structure of $Fe_2O_3$ not only increased the light harvesting efficiency because of its multiple scattering and slow-photon effect, but also enhanced the separation efficiency of generated holes and electrons. In another world, 3DOM–$Fe_2O_3$ would generate more electrons and holes under visible light irradiation, which then migrated to the surface of 3DOM–$Fe_2O_3$/CA electrode. The formed holes would directly oxidize the organic pollutant to intermediate products [49,50] for improving TOC removal (Eq. (9)). In turn, electrons were participated in Reactions (1) and (5), besides, were also captured by $H_2O_2$ to generate •OH through Reaction (10) [51], inhibiting the recombination of holes and electrons.

$$3DOM\text{–}Fe_2O_3 + h\nu \rightarrow h^+ + e^- \quad (8)$$

$$h^+ + IMI \rightarrow \text{intermediateproduct} \quad (9)$$

$$H_2O_2 + e^- \rightarrow OH + OH^- \quad (10)$$

### 3.4. Excellent chemical reusability and stability of IMI degradation

From the view of actual application, the catalyst stability is an important issue that has to be considered. Therefore, the iron leaching ($C_{Fe3+}$) from 3DOM–$Fe_2O_3$/CA and common $Fe_2O_3$/CA electrodes was detected during the SPEF process, as shown in Fig. 17. The results presented that the $C_{Fe3+}$ of both electrodes continuously increased with increasing the degradation time. Whereas, the $C_{Fe3+}$ was only 0.3 mg $L^{-1}$ for 3DOM–$Fe_2O_3$/CA electrode in 4 h, which is acceptable according to EC discharge stands (<2 ppm). Additionally, 3DOM–$Fe_2O_3$/CA possessed much lower iron leaching degree than common $Fe_2O_3$/CA electrode (i.e., 1.2 mg $L^{-1}$ at 4 h). This means the treated contaminants can be directly discharged into the sewage system. Therefore, it would be more cost-effective and practicable in a plant-scale operation with this novel 3DOM–$Fe_2O_3$/CA electrode especially at neutral pH.

The variations of pH during the EF and SPEF oxidation processes were indicated, as shown in Fig. 18. The changes of pH were very little, which is benefit for the stability of cathode. During EF and SPEF reaction, active oxygen molecules were adsorbed on the surface of 3DOM–$Fe_2O_3$/CA cathode and then transformed to hydrogen peroxide through in situ reduction with two electrons captured in the circuit (Eq. (1)). This process requires constant consumption of $H^+$ in water. Meanwhile, the surface iron species (Fe(III)–OH) interacted with formed $H_2O_2$ to generate $H^+$ (Eqs. (2)–(4)). So

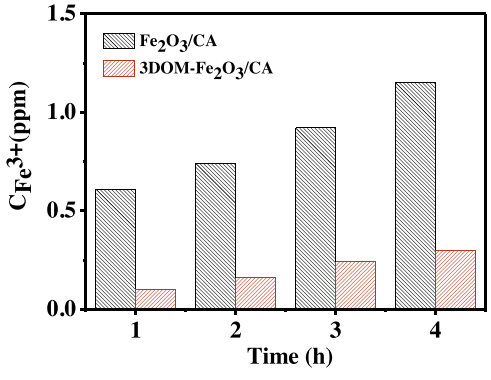


**Fig. 17.** The concentration of iron leaching in solution during SPEF oxidation of imidacloprid process at neutral condition.

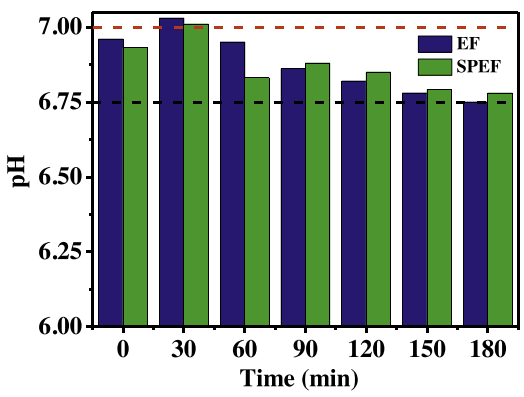


**Fig. 18.** The changes of pH during the EF and SPEF oxidation processes.

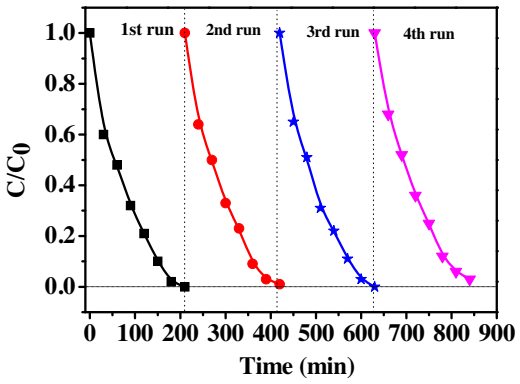


**Fig. 19.** Degradation of imidacloprid (200 ppm) in different batch runs over 3DOM–$Fe_2O_3$/CA–SPEF system.

the pH of solution can be maintained at relatively stable value (6.75–7.0).

Unfortunately, the reusability is another key issue for the application of catalyst in economic perspective. The recycling capability of 3DOM–$Fe_2O_3$/CA was successfully evaluated by degrading IMI over the reused cathode in SPEF process, as exhibited in Fig. 19. The degradation efficiency almost remained the same as fresh sample after 850 min recycling utilization. The obtained results demonstrated that the fabricated 3DOM–$Fe_2O_3$/CA electrode possessed good stability, which has a great potential for long-term practical application.

## 4. Conclusions

Novel 3DOM–$Fe_2O_3$/CA electrode was successfully fabricated by combination with the sol–gel and hard template (PS spheres) method based on self-assembled photonic crystal. The obtained cathode was further proposed in SPEF process for efficiently degradation of imidacloprid at neutral pH. The SEM results exhibited that the average macropore size of 3D-ordered $Fe_2O_3$ is around 390–425 nm and the holes with the diameter of ~120 nm in each layer formed a hollow "cyclindrical tube" in the vertical direction. In SPEF process, the IMI removal efficiency with 3DOM–$Fe_2O_3$/CA electrode was 95% at 2.5 h, with respect to 74% with reference $Fe_2O_3$/CA electrode. The kinetic analysis showed that the degradation of IMI follows the pseudo-first order regardless of electrode. The apparent rate constant for 3DOM–$Fe_2O_3$/CA electrode is 0.326 $h^{-1}$, increased 97% by comparing to $Fe_2O_3$/CA that of 0.165 $h^{-1}$. The energy consumed (EC) in SPEF system with novel 3DOM–$Fe_2O_3$/CA was used more effectively for IMI degradation. The improved degradation efficiency with 3DOM–$Fe_2O_3$/CA was owing to the improved Fenton and photocatalytic ability. EPR and radical trapping experiments revealed that the •OH radicals were main oxidants in SPEF system and 3D-ordered macroporous structure favoring the formation of •OH. The enhanced photocatalytic acitivity with 3D-macroporous structure is attributed to the improved light harvesting efficiency, efficient mass transport and slow photon effect under visible light irradiation. This study provides new insight of controlling structure to improve photoelectro-Fenton activity at neutral pH and 3DOM–$Fe_2O_3$/CA electrode is promising to be potentially used in organic pollutants removal in wastewater.

## Acknowledgements

This work was supported jointly by the National Natural Science Foundation P.R. China (Project no. 21277099, 21207101), Science & Technology Commission of Shanghai Municipality (14DZ2261100) and the Fundamental Research Funds for the Central Universities.

## References

[1] P.V. Nidheesh, R. Gandhimathi, Desalination 299 (2012) 1–15.
[2] E. Brillas, J. Braz. Chem. Soc. 25 (2014) 393–417.
[3] O. Iglesias, J. Gómez, M. Pazos, M.Á. Sanromán, Appl. Catal. B: Environ. 144 (2014) 416–424.
[4] Y. Wang, Y. Liu, X.-z. Li, F. Zeng, H. Liu, Sep. Purif. Technol. 106 (2013) 32–37.
[5] Y. Wang, H. Zhao, J. Gao, G. Zhao, Y. Zhang, Y. Zhang, J. Phys. Chem. C 116 (2012) 7457–7463.
[6] M. Pera-Titus, V. Garcíía-Molina, M.A. Baños, J. Giménez, S. Esplugas, Appl. Catal. B: Environ. 47 (2004) 219–256.
[7] Z. Ai, T. Mei, J. Liu, J. Li, F. Jia, L. Zhang, J. Qiu, J. Phys. Chem. C 111 (2007) 14799–14803.
[8] M. Panizza, G. Cerisola, Chem. Rev. 109 (2009) 6541–6569.
[9] F.C. Moreira, R.A.R. Boaventura, E. Brillas, V.J.P. Vilar, Appl. Catal. B: Environ. 162 (2015) 34–44.
[10] A. Özcan, Y. Şahin, A.S. Koparal, M.A. Oturan, Appl. Catal. B: Environ. 89 (2009) 620–626.
[11] A. Dhaouadi, N. Adhoum, Appl. Catal. B: Environ. 97 (2010) 227–235.
[12] C.K. Duesterberg, T.D. Waite, Environ. Sci. Technol. 40 (2006) 4189–4195.
[13] M. Hermanek, R. Zboril, I. Medrik, J. Pechousek, C. Gregor, J. Am. Chem. Soc. 129 (2007) 10929–10936.
[14] A. Cabrera Reina, L. Santos-Juanes, J.L. García Sánchez, J.L. Casas López, M.I. Maldonado Rubio, G. Li Puma, J.A. Sánchez Pérez, Appl. Catal. B: Environ. 166–167 (2015) 295–301.
[15] E. Brillas, I. Sires, M.A. Oturan, Chem. Rev. 109 (2009) 6570–6631.
[16] C. Ruales-Lonfat, J.F. Barona, A. Sienkiewicz, M. Bensimon, J. Vélez-Colmenares, N. Benítez, C. Pulgarín, Appl. Catal. B: Environ. 166–167 (2015) 497–508.
[17] H. Xie, Y.Z. Li, S.F. Jin, J.J. Han, X.J. Zhao, J. Phys. Chem. C 114 (2010) 9706–9712.
[18] R.Z. Zhang, H.X. Dai, Y.C. Du, L. Zhang, J.G. Deng, Y.S. Xia, Z.X. Zhao, X. Meng, Y.X. Liu, Inorg. Chem. 50 (2011) 2534–2544.
[19] A. Stein, R.C. Schroden, Curr. Opin. Solid State Mater. Sci. 5 (2001) 553–564.
[20] G.Q. Guan, R. Zapf, G. Kolb, Y. Men, V. Hessel, H. Loewe, J.H. Ye, Chem. Commun. (3) (2007) 260–262.
[21] S.A. Steiner, T.F. Baumann, J. Kong, J.H. Satcher, M.S. Dresselhaus, Langmuir 23 (2007) 5161–5166.
[22] M.A. Worsley, J.H. Satcher Jr., T.F. Baumann, Langmuir 24 (2008) 9763–9766.
[23] F.C. Moreira, S. Garcia-Segura, R.A.R. Boaventura, E. Brillas, V.J.P. Vilar, Appl. Catal. B: Environ. 160–161 (2014) 492–505.
[24] S.Y. Yuan, Y. Fan, Y.C. Zhang, M. Tong, P. Liao, Environ. Sci. Technol. 45 (2011) 8514–8520.
[25] P. Jeschke, R. Nauen, M. Schindler, A. Elbert, J. Agric. Food Chem. 59 (2011) 2897–2908.
[26] Y.N. Jin, G.H. Zhao, M.F. Wu, Y.Z. Lei, M.F. Li, X.P. Jin, J. Phys. Chem. C 115 (2011) 9917–9925.
[27] M.F. Wu, Y.N. Jin, G.H. Zhao, M.F. Li, D.M. Li, Environ. Sci. Technol. 44 (2010) 1780–1785.
[28] Z.C. Zhou, X.S. Zhao, Langmuir 20 (2004) 1524–1526.
[29] N.P. Liu, J. Shen, D. Liu, Electrochim. Acta 97 (2013) 271–277.
[30] Y.J. Wang, H.Y. Zhao, S.N. Chai, Y.B. Wang, G.H. Zhao, D.M. Li, Chem. Eng. J. 223 (2013) 524–535.
[31] Y.B. Wang, H.Y. Zhao, G.H. Zhao, Appl. Catal. B: Environ. 164 (2015) 396–406.
[32] L. Xu, J. Wang, Appl. Catal. B: Environ. 123 (2012) 117–126.
[33] S.N. Chai, G.H. Zhao, Y.J. Wang, Y.N. Zhang, Y.B. Wang, Y.F. Jin, X.F. Huang, Appl. Catal. B: Environ. 147 (2014) 275–286.
[34] Y.N. Jin, M.F. Wu, G.H. Zhao, M.F. Li, Chem. Eng. J. 168 (2011) 1248–1255.
[35] H.Y. Zhao, Y.J. Wang, Y.B. Wang, T.C. Cao, G.H. Zhao, Appl. Catal. B: Environ. 125 (2012) 120–127.
[36] K. Ji, J. Deng, H. Zang, J. Han, H. Arandiyan, H. Dai, Appl. Catal. B: Environ. 165 (2015) 285–295.
[37] J.F. Galisteo-Lopez, M. Ibisate, R. Sapienza, L.S. Froufe-Perez, A. Blanco, C. Lopez, Adv. Mater. 23 (2011) 30–69.
[38] Y. Wang, W.P. Du, Y.M. Xu, Langmuir 25 (2009) 2895–2899.
[39] E. Cuinea, F. Centellas, J.A. Garrido, R.M. Rodríguez, C. Arias, P.L. Cabot, E. Brillas, Appl. Catal. B: Environ. 89 (2009) 459–468.
[40] L.D. Sánchez, S.F.M. Taxt-Lamolle, E.O. Hole, A. Krivokapić, E. Sagstuen, H.J. Haugen, Appl. Catal. B: Environ. 142–143 (2013) 662–667.
[41] D. Tsukamoto, Y. Shiraishi, Y. Sugano, S. Ichikawa, S. Tanaka, T. Hirai, J. Am. Chem. Soc. 134 (2012) 6309–6315.
[42] T.L. Thompson, J.T. Yates, J. Phys. Chem. B 109 (2005) 18230–18236.
[43] T.L. Xu, Y. Cai, K.E. O'Shea, Environ. Sci. Technol. 41 (2007) 5471–5477.
[44] H. Zhang, R.L. Zong, Y.F. Zhu, J. Phys. Chem. C 113 (2009) 4605–4611.
[45] S.S. Lin, M.D. Gurol, Environ. Sci. Technol. 32 (1998) 1417–1423.
[46] B.R. Petigara, N.V. Blough, A.C. Mignerey, Environ. Sci. Technol. 36 (2002) 639–645.
[47] A.L.T. Pham, F.M. Doyle, D.L. Sedlak, Environ. Sci. Technol. 46 (2012) 1055–1062.
[48] C.C. Wang, J.R. Li, X.L. Lv, Y.Q. Zhang, G. Guo, Energy Environ. Sci. 7 (2014) 2831–2867.
[49] A. Mills, R.H. Davies, D. Worsley, Chem. Soc. Rev. 22 (1993) 417–425.
[50] K. Hashimoto, T. Kawai, T. Sakata, J. Phys. Chem. 88 (1984) 4083–4088.
[51] K. Villa, S. Murcia-López, T. Andreu, J.R. Morante, Appl. Catal. B: Environ. 163 (2015) 150–155.